

Tuneable structure and magnetic properties in $\text{Fe}_{3-x}\text{V}_x\text{Ge}$ alloysR. Mahat^{a,*}, Shambhu KC^a, D. Wines^b, F. Ersan^{b,c}, S. Regmi^a, U. Karki^a, R. White^d, C. Ataca^b, P. Padhan^e, A. Gupta^f, P. LeClair^{a,**}^a Department of Physics and Astronomy, University of Alabama, Tuscaloosa, AL, 35487, USA^b Department of Physics, University of Maryland Baltimore County, Baltimore, MD, 21250, USA^c Department of Physics, Aydin Adnan Menderes University, Aydin, 09100, Turkey^d Department of Metallurgical & Materials Engineering, University of Alabama, Tuscaloosa, AL, 35487, USA^e Department of Physics, Nanoscale Physics Laboratory, Indian Institute of Technology Madras, Chennai, 600036, India^f Department of Chemistry and Biochemistry, The University of Alabama, Tuscaloosa, AL, 35487, USA

ARTICLE INFO

Article history:

Received 17 October 2019

Received in revised form

13 February 2020

Accepted 16 February 2020

Available online 25 February 2020

Keywords:

spintronics

Half-metals

Heuslers

Ferromagnets

Crystal structure

Martensitic phase transformation

Electrical conductivity

Vickers micro hardness

Ab initio calculations

ABSTRACT

We report a detailed experimental and theoretical study of the effects of V substitution for Fe atom on the structural, magnetic, transport, electronic and mechanical properties of an off-stoichiometric $\text{Fe}_{3-x}\text{V}_x\text{Ge}$ intermetallic alloy series ($0 \leq x \leq 1$). Single phase microstructures are observed for $x < 0.75$, whereas higher V content alloys $x \geq 0.75$ are multi-phased. Vanadium substitution is observed to induce a diffusionless martensitic phase transformation from a Heusler-like L_{21} structure to hexagonal DO_{19} structure, as corroborated by Differential Scanning Calorimetry results. The vanadium substitution is also found to decrease the grain size, inhibiting the grain growth by pinning the grain boundary migration. All the alloys in the series are found to be soft ferromagnets at 5 K with saturation magnetic moment and Curie temperature decreasing as V concentration increases. The low temperature saturation magnetic moment is in close agreement with the expected Slater-Pauling values for the L_{21} phases, while the hexagonal samples have markedly higher values of saturation moments. First-principle calculations agree with the experimental findings and reveal that V substitution energetically favours one of the Fe sites in Fe_3Ge . The electrical resistivity measured over the temperature range from 5 K to 400 K shows negative temperature coefficient of resistivity at high temperatures with increasing the V concentration. Relatively high mechanical hardness values are also observed, with the values increasing with increasing V content. Vanadium substitution is found to play a central role in tuning the mechanical properties, stabilising the L_{21} structure, and shifting the martensitic transformation temperature to higher values from that of parent Fe_3Ge .

© 2020 Elsevier B.V. All rights reserved.

1. Introduction

Heusler alloys, first discovered by and named after Fritz Heusler in 1903 [1], are very useful for applications in information storage and spintronics as well as many other areas [2–7]. For applications in magnetism and spintronics [2], the inherently low magneto-crystalline anisotropy in cubic Heusler alloys can be limiting factor [8]. Identifying a hexagonal Heusler analogue [3] that retains half metallicity and exhibits a high magneto-crystalline anisotropy may

be very attractive for applications such as perpendicular media, current perpendicular to plane giant magnetoresistance (CPP-GMR), and spin-torque-transfer RAM (STT-RAM) [9–13]. However, half-metallicity has been predicted for some Heusler analogues in the hexagonal DO_{19} ($\text{P6}_3/\text{mmc}$, space group no. 194 [14,15]) crystal structure [3,16,17].

The intermetallic compound Fe_3Ge is well known to crystallize in two crystal structures, a cubic L_{12} phase ($\text{Pm}\bar{3}\text{m}$, space group no. 221 [14,15]) at low temperatures ($< 700^\circ\text{C}$) and hexagonal DO_{19} phase at higher temperatures ($> 700^\circ\text{C}$) [18,19]. In this compound, the forward L_{12} to DO_{19} structural transformation takes place easily but the reverse DO_{19} to L_{12} transformation is difficult to achieve under normal cooling conditions, and often one retains the high temperature DO_{19} crystal structure [19–21]. A few attempts have been made in the past on the substitution of V for Fe atom in Fe_3Ge

* Corresponding author.

** Corresponding author.

E-mail addresses: rmahat@crimson.ua.edu (R. Mahat), pleclair@ua.edu (P. LeClair).

alloy and structural transformations are studied. Nakagawa and Kanematsu [22], by means of X-ray and magnetic studies have suggested the hexagonal DO₁₉ phase of parent Fe₃Ge transforms to a body centred cubic (A2) structure for $x \geq 0.50$. They have reported the structure to be A2 due to the absence of superlattice peaks in X-ray diffraction. However, later Beitollahi and Booth [23] have reported structure to be L2₁ ($Fm\bar{3}m$, space group no. 225 [14,15]) based on the presence of (111) superlattice peak in their room temperature neutron diffraction patterns for nominally single phase samples with $x \geq 0.60$. In spite of several investigations [22,23] aimed at understanding the structural phase transformation, the detailed mechanisms responsible for such transformations are still far from being understood. Further, they lack any microstructural analysis. Large magneto-optical Kerr rotations have also been observed in the same system [24].

To our best knowledge, there is not yet a detailed report of the structural, magnetic, transport, and mechanical properties of Fe_{3-x}V_xGe in the bulk form, neither experimentally nor theoretically. Previous investigations focused on substituting V in one of Fe site in Fe₃Ge under higher temperature annealing conditions. Reports on low temperature annealing conditions are not available thus far. In this study, we have addressed different annealing conditions and systematically studied the microstructure and phase purity, magnetic properties, electrical transport, differential scanning calorimetry, and hardness in addition to structure determination to understand the structure-property relationships in this interesting family of Heusler-like compounds. Particular attention has been paid to metallography and microstructural analysis to determine which regions of the phase diagram yield single phase specimens.

2. Experimental details

Fe_{3-x}V_xGe ($0 \leq x \leq 1$) bulk samples with x varying in the steps of 0.125, were prepared by arc melting of stoichiometric amounts of the constituents in an argon atmosphere at 10^{-4} mbar (see details in Supplementary Information). Care was taken to avoid oxygen contamination. As an oxygen getter, Ti was melted inside the vacuum chamber separately before melting the compound to avoid oxygen contamination. The as-cast ingots were examined repeatedly using scanning electron microscopy (SEM) and energy dispersive X-ray spectroscopy (EDS) analysis in a JEOL 7000 Field Emission Scanning Electron Microscope (FESEM) to confirm homogeneity and correct composition. After confirming the anticipated target composition, the polycrystalline ingots were then annealed in an evacuated quartz tube at different temperatures ranging from 650 °C to 1000 °C for different dwell times (5 days–25 days), and at the end of each annealing cycle, the samples were cooled slowly in the furnace to get optimum crystallisation to promote the formation of L2₁ structure.

Annealed ingots were polished for spectroscopic investigations (see details in Supplementary Information). The polishing was done, first grinding using silicon carbide abrasive discs (120 through 1200 grit size) followed by diamond suspension polishing. Colloidal silica suspension of grit size 0.02 μm was used at last for the finest polishing. After obtaining a smooth and reflective surface, the samples were etched with Adler etchant (9 g of CuNH₃Cl, 45 g of hydrated FeCl₂, 150 mL of HCl and 75 mL of DI Water) [25]. The purpose of etching is that etchant attacks different phases present in the samples at different rates, and provides high quality surface contrast for microstructure characterisation.

The crystal structure was investigated by means of X-ray diffraction (XRD) using a Bruker D8 Discover X-ray diffractometer equipped with monochromatic Co-K α ($\lambda = 0.179$ nm) radiation. The polished samples were rotated around the ϕ axis during the XRD

measurement to minimise surface effects. CaRIne crystallography 4.0 software [26] as well as in-house PYTHON code [27] including the dispersive corrections to the atomic scattering factors were used to simulate the XRD patterns to compare with the experimental XRD patterns. XRD analysis (Rietveld refinement) was done using the CRYSTAL IMPACT MATCH! software based on the FULLPROF algorithm [28] that uses the least-square refinement between experimental and calculated intensities. The crystal structures determined from XRD were further confirmed using electron backscatter diffraction (EBSD) phase mapping analysis in a JEOL 7000 FESEM system. The low temperature magnetic and electrical transport properties were studied in Quantum Design Physical Properties Measurement System (PPMS), while the high temperature magnetisation was measured using the Lakeshore VSM 7410. DSC measurements were carried out to confirm the diffusionless martensitic transformation (with a ramp rate 10 °C/min during heating and cooling) in the temperature range up to 1200 °C in a Setaram Labsys Evo. in Ar gas flux at the rate of 20 mL/min to prevent the possible oxidation of the samples. The temperature and the heat reaction were calibrated using high purity indium, aluminium, silver and nickel standards. The mechanical properties were studied in terms of Vicker's hardness by using Buehler model 1600–6100 micro-hardness tester.

3. Experimental results and discussions

3.1. Microstructural and compositional analysis

XRD is not always sufficient to confirm the phase purity if the impurity phase content is less than 5% of the overall volume [29,30]. In such case, optical microscopy and SEM of polished and etched samples are the most direct ways to characterise microstructure by revealing grain boundaries, phase boundaries, and inclusion distribution. Observing different contrast in etched sample seen from optical microscopy, we can speculate the presence of impurity phases, and SEM with EDS/EBSD can be used to directly quantify whether areas of different contrast represent impurity phases or possible different crystallite orientations.

Starting from the fully stoichiometric Fe₂VGe, multi-phase microstructure was obtained in every heat treatment performed at 800, 900, 950, or 1000 °C for different dwelling times; 3, 5, 7, or 14 days. However, with the substitution of Fe for V, the secondary phase began to disappear and uniform single phase behaviour was observed in the V composition range ($0 \leq x \leq 0.625$). All other higher V concentration produced multiphase behaviour (see details in Supplementary Information). Fig. 1 shows microstructure of all single phase samples observed under high temperature annealing conditions i.e., 7 days at 950 °C using optical microscope. The microstructure of the high temperature (> 700 °C) phase for $x = 0$ i.e., the parent Fe₃Ge compound is also presented in Fig. 1 already known to be stable, annealed under similar conditions [19–21].

In addition to high temperature annealing, we also attempted to investigate low temperature annealing of our V-substituted alloys (see details in Supplementary Information) to check if the samples which showed single phase microstructure at high temperature annealing conditions were indeed stable at low temperature as well, as low temperature annealing is missing in previous works. Low temperature annealing is also necessary to shed more light on the structural phase transformation as this alloy series is reported to show structural phase transformation from low temperature L1₂ or L2₁ to high temperature DO₁₉ phase, similar to parent Fe₃Ge [19–21]. Single phase granular microstructures was observed for the intermediate compositions $x = 0.50$ and 0.25 . In the case of Fe₃Ge ($x = 0$), small amounts of secondary phases were observed in agreement with detailed studies on the parent Fe₃Ge compound

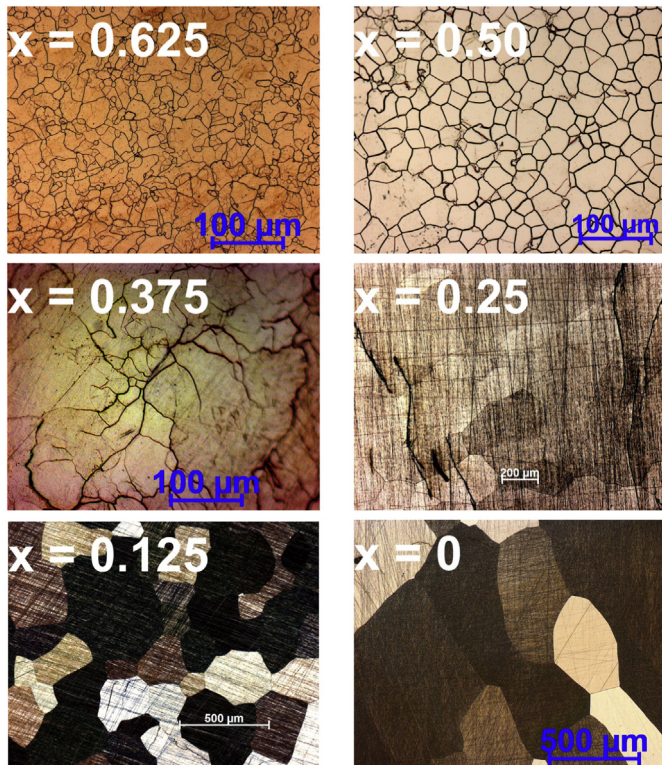


Fig. 1. Optical micrograph of $\text{Fe}_{3-x}\text{V}_x\text{Ge}$ ($0 \leq x \leq 1$) heat treated at 950°C for 7 days showing the grain structures. The samples were etched for 25 s using the Adler etchant.

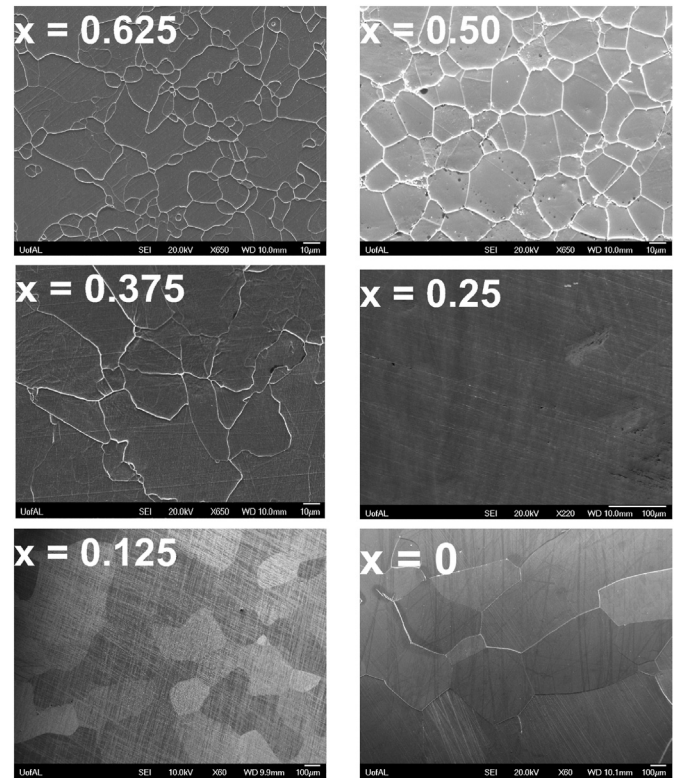


Fig. 2. SEM micrograph of $\text{Fe}_{3-x}\text{V}_x\text{Ge}$ ($0 \leq x \leq 1$) heat treated at 950°C for 7 days showing the granular microstructure. The magnification of each micrograph is indicated at the bottom, like $\times 650$ for $x = 0.50$.

[8,20,22]. The composition of all the stable single phase samples in the series are confirmed to be close to the target composition within $\sim 5\%$ instrumental uncertainty range using EDS (see details in Supplementary Information).

Fig. 2 shows the SEM images displaying the microstructure of all single phase samples (see Supplementary Information for SEM images of low temperature annealed samples). Relatively small grains are observed compared to high temperature annealed samples. The effect of V substitution on the microstructure is substantial. The average grain size is observed to decrease dramatically with increasing the V content indicating the V substitution can effectively inhibit the grain boundary migration. The dramatic increase in grain size with decreasing V content is also accompanied by the increase of roughness of certain grains, producing different color contrast between neighbouring grains in bright-field as reported in the literatures [31,32].

3.2. Crystal structure and atomic order analysis

Fig. 3 (a) shows the XRD patterns of the $\text{Fe}_{3-x}\text{V}_x\text{Ge}$ alloy series annealed at 950°C for 7 days after polishing and etching, using a Co- $\text{K}\alpha$ radiation source. The crystal structure obtained from the XRD data suggests the presence of L2_1 Heusler structure for $0.375 \leq x \leq 0.75$ and hexagonal DO_{19} structure for $0 \leq x \leq 0.25$, whereas the intermediate composition $\text{Fe}_{2.6875}\text{V}_{0.3125}\text{Ge}$ showed the co-existence of both phases and onset of structural phase transformation (see Fig. 3(a) fourth row from the top). Fig. 3(c) shows the XRD pattern of $\text{Fe}_{3-x}\text{V}_x\text{Ge}$ alloys series annealed at 650°C for 25 days. Interestingly, for the lower temperature annealing it showed Heusler like L2_1 ordering for $x = 0.25$, while at higher temperature annealing it showed DO_{19} ordering. The low temperature cubic L1_2 crystal phase of the parent Fe_3Ge compound is also observed with

some impurity peaks (represented by asterisks) with lattice constant $a = 3.6667\text{\AA}$ as reported in the literature [33].

For all cubic single-phase compositions $0.375 \leq x \leq 0.75$, only three distinct Heusler-like reflection peaks (h, k, l all odd or even) are observed; fundamental peaks with $h + k + l = 4n$, even superlattice peaks with $h + k + l = 4n + 2$ and odd superlattice peaks $h + k + l = 2n + 1$. In Heusler-like alloys, presence of (111) peak indicates the chemical ordering of atoms in octahedral positions, and (200) peak reflects the superlattice reflections due to atoms in tetrahedral positions, while (220) peak is a principal reflection. None of the low angle superlattice peaks are absent in all cubic structures which indicates a degree of sublattice ordering. No mixed odd/even indices are observed in reflection peaks indicating that all cubic samples are crystallised in the face-centred cubic Heusler-like structure. The intensity of superlattice peak (111) is greater than that of (200) peak in all stable cubic phases consistently, though as noted below texturing effects make it difficult to rely on XRD peak intensities.

Considering the fact that Heusler-like compounds can crystallize in a number of structures, particularly the ordered L2_1 ($Fm\bar{3}m$, space group no. 225 [14,15]) and X_a ($F\bar{4}3m$, space group no. 216 [14,15]) as well as the disordered A2 and B2 phases, structure assignment should be undertaken carefully. We can argue here that there is no complete A2 and B2 disorder on the basis of presence of low angle superlattice peaks in all stable cubic compositions. Furthermore, the distinction between L2_1 and X_a structure is rather challenging from X-ray diffraction experiment if the participating elements in the alloy have similar X-ray scattering properties.

However, Beitollahi and Booth [23] previously proposed an L2_1 structure for $x = 0.6$ to 1.0, which we corroborate here (see Table 1). Our construction of possible structures is as follows; starting from

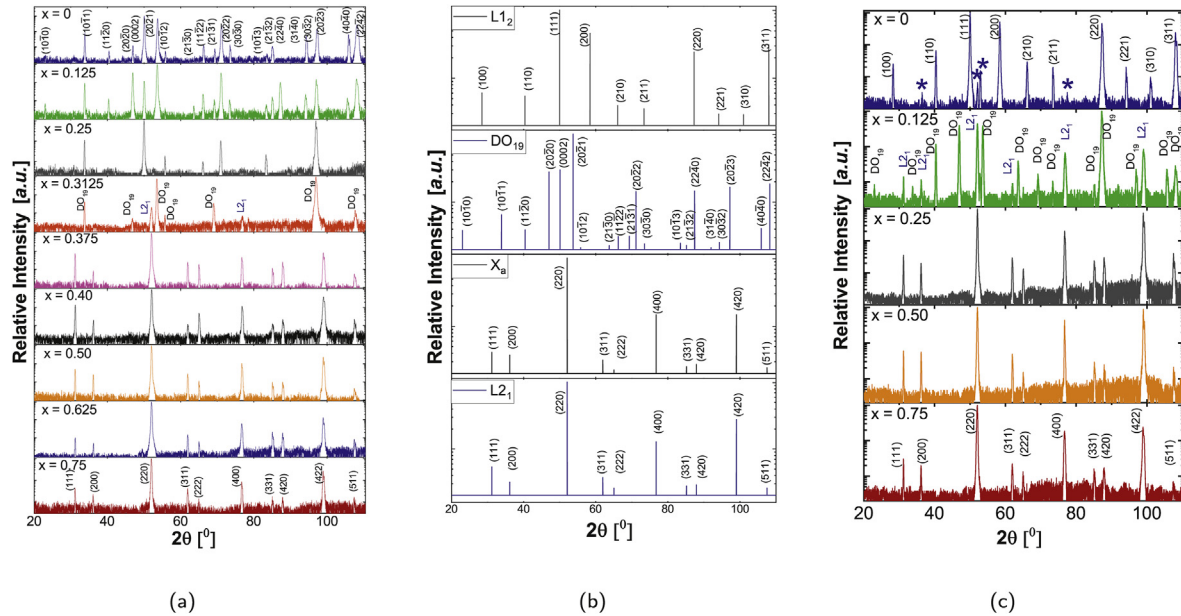


Fig. 3. Experimental XRD patterns of $\text{Fe}_{3-x}\text{V}_x\text{Ge}$ alloy series annealed at (a) 950 °C for 7 days and (c) 650 °C for 25 days using X-ray source, and (b) simulated powder XRD patterns using CaRIne. For (a), the upper indexing is for the DO_{19} structure and the lower indexing is for the L_{21} structure. For (c), the upper indexing is for the L_{12} structure and the lower indexing is for the L_{21} structure.

Table 1

Possible site assignments for cubic $\text{Fe}_{3-x}\text{V}_x\text{Ge}$ assuming two space groups; L_{21} ($Fm\bar{3}m$) and X_a ($F\bar{4}3m$).

Type	Ge	$\text{Fe}_{1-x}\text{V}_x$	Fe	Fe
L_{21}	4a (0,0,0)	4b $\begin{pmatrix} 1 & 1 & 1 \\ 2 & 2 & 2 \end{pmatrix}$	8c $\begin{pmatrix} 1 & 1 & 1 \\ 4 & 4 & 4 \end{pmatrix}$	8c $\begin{pmatrix} 1 & 1 & 3 \\ 4 & 4 & 4 \end{pmatrix}$
X_a	4a (0,0,0)	4c $\begin{pmatrix} 1 & 1 & 1 \\ 4 & 4 & 4 \end{pmatrix}$	4b $\begin{pmatrix} 1 & 1 & 1 \\ 2 & 2 & 2 \end{pmatrix}$	4d $\begin{pmatrix} 3 & 3 & 3 \\ 4 & 4 & 4 \end{pmatrix}$

parent Fe_3Ge compound, where Fe atoms occupy 4b and 8c (or 4c and 4d) sites whereas Ge atom fills 4a site. In this picture, the substituted V atom can have several possible ways to fill the crystal structure; it can replace the Fe atom on 4b site, or 4c site, or 4d site. It is also possible for V atom to replace Ge atom to other site and fill the vacant position, however in the experimental XRD pattern we confirm that the Ge atoms form an *fcc* superstructure on the underlying *bcc* superlattice. Hence, we argue that 4a site is completely ordered. Further, the replacement of Fe atom on 4c and 4d site doesn't alter the X-ray intensity as these sites belong to the same sublattice (with octahedral symmetry). In view of this, we are left with two possibilities and we try to push further XRD based analysis to shed light on the exact atomic order of the alloys. To further narrow down the exact atomic ordering, we simulated the XRD patterns for $\text{Fe}_{2.50}\text{V}_{0.50}\text{Ge}$ considering different crystal structures (see Fig. 3(b)). The experimental XRD pattern observed matches to L_{21} structure generated in either CaRIne 4.0 simulations or CRYSTAL IMPACT MATCH, or our in-house python code for $\text{Fe}_{2.50}\text{V}_{0.50}\text{Ge}$. The superlattice peaks (111) and (200) have a little bit higher intensity than those generated from simulations, which might be due to texturing effects, given the large grain size we observe ($\sim 30 \mu\text{m}$). As the crystal structure of parent Fe_3Ge is hexagonal DO_{19} at higher temperature ($> 700^\circ\text{C}$) and cubic (L_{12}) at lower temperature ($< 700^\circ\text{C}$), the L_{12} crystal structure was also simulated using CaRIne 4.0 software, but none of the intensities and peak positions matched with the experimental pattern (see Fig. 3(b)).

Rietveld refinement shows good agreement (reduced $\chi^2 = 1.4$ and weighted average Bragg R -factor = 3.6) between the observed

XRD pattern and the calculated pattern for the L_{21} (space group 225) structure with the experimental lattice parameter $a = 5.7632\text{\AA}$ as shown in Fig. 4(a). The goodness of fit parameters (reduced $\chi^2 = 5.2$ and weighted average Bragg R -factor = 9.7) are always higher for X_a (space group 216) structure considered in Table 1. Having no evidence to the contrary, we presume Fe and V mix randomly on the 4b sites. This is also in good agreement with the Pauling electronegativity rule. Because V and Ge have a higher electronegativity difference, they will tend to form a rock-salt (NaCl) type lattice and coordinate octahedrally due to ionic nature of their interactions. EBSD inverse pole figure (IPF) map and phase map of $\text{Fe}_{2.50}\text{V}_{0.50}\text{Ge}$ were also performed to determine the degree of texturing and purity of phase considered. Relatively large grains with some preferred orientation is revealed from IPF as shown in Fig. 4(b). Almost 95% of the selected microstructure is observed to match the proposed L_{21} structure (red color in the EBSD map (see Fig. 4(c)) with some zero solution regions (black spots) mainly in grain boundaries due to the artefact of polishing and some nominal Ge segregation. All these experimentally observed facts support that the crystal structure of all stable cubic samples $0.375 \leq x \leq 0.75$ is L_{21} , in agreement with Beitollahi and Booth [23]. The L_{21} structure is shown in Fig. 5(a).

In order to determine the atomic ordering in hexagonal samples, $x = 0.125$ is chosen for Rietveld refinement due to the visibility of all hexagonal peaks in XRD. Even though the texturing effect from larger grains ($\sim 300 \mu\text{m}$) is evident in peak intensities, a final reduced $\chi^2 = 7.7$ is found. This single digit goodness of fit parameter between the observed XRD pattern and the calculated pattern for the hexagonal DO_{19} (space group 194) indicates the reliability of the fit (see Fig. 4(d)). According to Rietveld refinement, the 6h sites (with the parameter $y = 5/6$) are shared by Fe and V with occupancy 0.958 and 0.042, respectively, in agreement with the nominal composition, and the 2c sites are occupied by Ge. Again, with no evidence to the contrary, we presume that Fe and V mix randomly on the 6h sites. This DO_{19} structure is shown in Fig. 5(c). The proposed site assignments are summarised for DO_{19} $\text{Fe}_{3-x}\text{V}_x\text{Ge}$ in Table 2 [17].

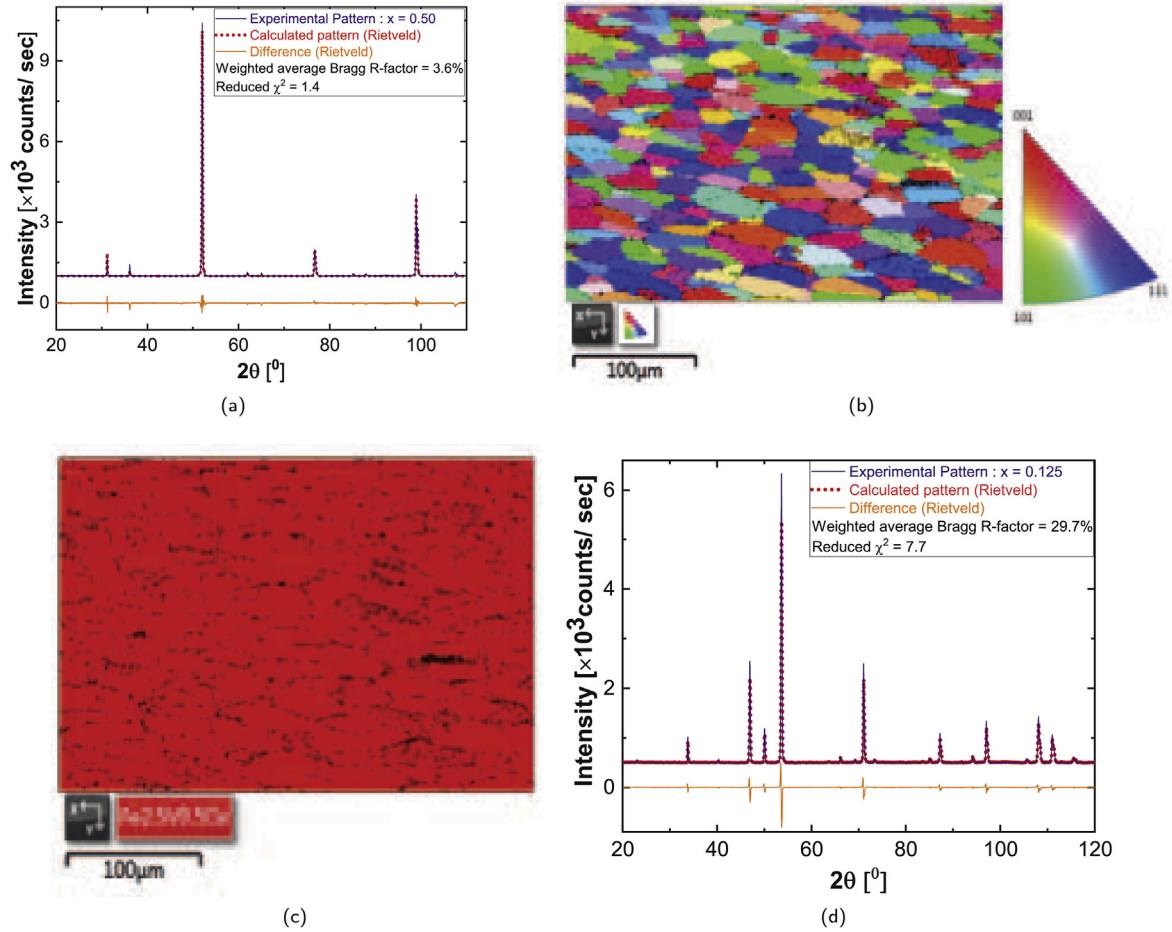


Fig. 4. (a) The Rietveld refinement of XRD pattern showing a signature of good fit with the proposed crystal model $L2_1$ (b) IPF color map (c) The corresponding EBSD phase color map of the same area of $Fe_{2.50}V_{0.50}Ge$ in SEM (d) The Rietveld refinement of XRD pattern for $Fe_{2.875}V_{0.125}Ge$ with the proposed DO_{19} crystal structure.

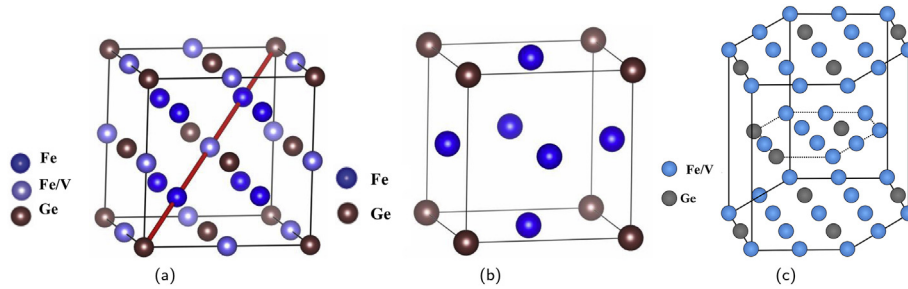


Fig. 5. Various crystal structures (a) $L2_1$, (b) $L1_2$, and (c) DO_{19} .

Table 2

Proposed site assignment for the hexagonal DO_{19} $Fe_{3-x}V_xGe$.

	Wyckoff position	Coordinates	Occupancy
Fe	$6h, y = \frac{5}{6}$	$(y, 2y, \frac{1}{4}) (-2y, -y, \frac{1}{4}) (y, -y, \frac{1}{4}) (-y, -2y, \frac{3}{4}) (2y, y, \frac{3}{4}) (-y, y, \frac{3}{4})$	$\frac{3-x}{3}$
V	$6h, y = \frac{5}{6}$	$(y, 2y, \frac{1}{4}) (-2y, -y, \frac{1}{4}) (y, -y, \frac{1}{4}) (-y, -2y, \frac{3}{4}) (2y, y, \frac{3}{4}) (-y, y, \frac{3}{4})$	$\frac{x}{3}$
Ge	$2c$	$(\frac{1}{3}, \frac{2}{3}, \frac{1}{4}) (\frac{2}{3}, \frac{1}{3}, \frac{3}{4})$	1

Lattice parameters of all cubic stable phases, calculated using Cohen's method with a Nelson-Riley error function [34], are observed to increase linearly with increasing V concentration (see Fig. 6(c)) which is expected according to Vegard's law [35] as the

lattice constant of bcc V (0.3024nm) is greater than that of bcc Fe (0.2867nm) [36]. Both lattice parameters a and c increase with the increase of V concentration for all hexagonal stable phases as shown in Fig. 6. The lattice parameters of all stable samples along

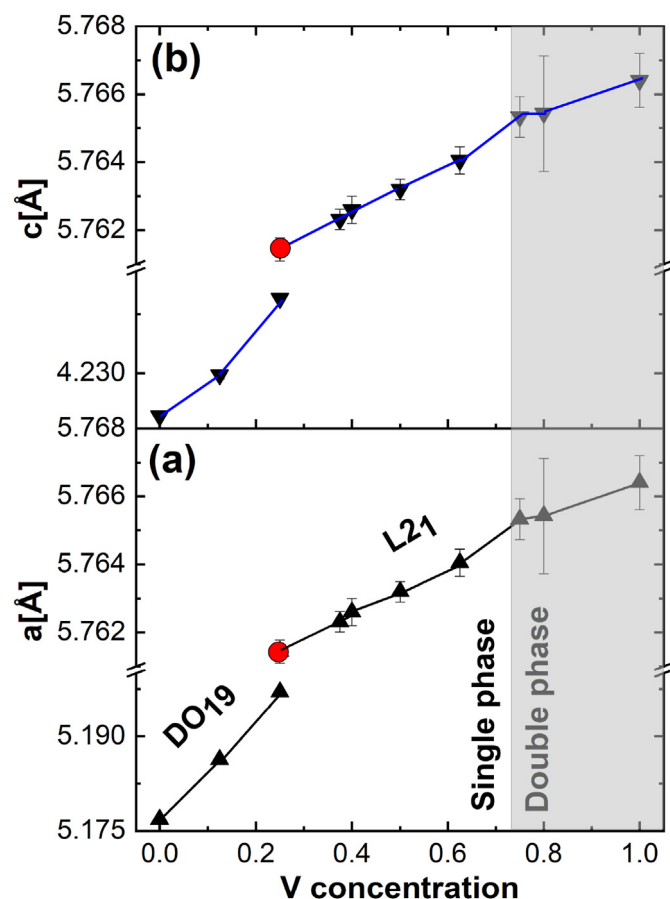


Fig. 6. Variation of lattice parameters of $\text{Fe}_{3-x}\text{V}_x\text{Ge}$ annealed at 950°C for 7 days (except the red data point representing $x = 0.25$ annealed at 650°C for 25 days) (a) a versus V concentration, and (b) c versus V concentration. The shaded region represents multiphase region.

with different annealing conditions for $\text{Fe}_{3-x}\text{V}_x\text{Ge}$ alloy series are presented in Table 3.

3.3. Phase transformation behaviour and thermal stability

Differential Scanning Calorimetry (DSC) is a simple but an

effective tool to identify phase transformation temperatures. Since the local composition of our samples does not change in going from one structure to another, this serves to indicate that the transformation is a diffusionless martensitic transformation, as observed in the parent compound Fe_3Ge . Continuous heating and cooling DSC curves of $\text{Fe}_{3-x}\text{V}_x\text{Ge}$ annealed at 950°C for 7 days measured at a heating/cooling rate of $10^\circ\text{C}/\text{min}$ are shown in Fig. 7(a). Fig. 7(b) shows the DSC curves at heating/cooling rate $10^\circ\text{C}/\text{min}$ for $x = 0$ and $x = 0.25$ annealed at 650°C for 25 days. The phase evolution is clearly seen from the DSC curves. The large, sharp endothermic peaks around 1120°C corresponds to the melting point which is in agreement with the reported melting point $\sim 1100^\circ\text{C}$ of parent Fe_3Ge . Additionally, small endothermic peaks are seen in addition to the prominent melting point peaks for all compositions having $L2_1$ structures, indicating the signature of first order phase transformations.

No peaks are observed in those compositions which were already crystallised in hexagonal DO_{19} structure at room temperature. Small endothermic peaks are also observed for $x = 0$ ($L1_2$) and $x = 0.25$ ($L2_1$) annealed at 650°C for 25 days during heating cycle only. All these experimentally observed facts indicate that transforming the $L1_2$ or $L2_1$ structure to the DO_{19} structure is relatively easy, but the reverse transition is relatively difficult for low V concentration [19,20]. Additionally, XRD on samples with $x = 0.25$ annealed at 950°C for 7 days and at 650°C for 25 days showed a DO_{19} structure and a $L2_1$ structure, respectively, corroborating the DSC measurements. Thus, we conclude that the small DSC peaks observed correspond to the structural phase transformation from cubic $L1_2$ or $L2_1$ to hexagonal DO_{19} . The linear shifting of the peak positions with increasing vanadium concentration, as shown in Fig. 7(c), indicates an improvement of the stability of the low temperature $L2_1$ structure with increasing V content. Notably, this low temperature $L2_1$ phase with V substitution is completely different from the low temperature $L1_2$ phase of the parent Fe_3Ge . The reproducibility of those peaks on cooling (with some hysteresis) and the lack of local composition variation suggests the transformation to be of the diffusionless martensitic type. We note that the hysteresis may be due to super-cooling (recall the heating/cooling rate of $10^\circ\text{C}/\text{min}$). The total entropy of phase transformation also changes significantly with V concentration (see Fig. 7(d)).

The onset temperatures (T_1), temperatures (T_p) and total entropy change (ΔS_p) of the phase transformation peaks, and melting points (T_m), measured at heating rate $10^\circ\text{C}/\text{min}$ for samples

Table 3
Experimental lattice parameters of $\text{Fe}_{3-x}\text{V}_x\text{Ge}$ alloy series of different crystal structures with annealing conditions, the experimental saturation magnetic moments at $T = 5\text{ K}$ along with the theoretical and Slater-Pauling (S-P) values, and the measured Curie temperature (T_c). The numbers in parentheses are the uncertainty in the last digit, e.g., $3.2(2) = 3.2 \pm 0.2$.

x	Crystal structure	Experimental lattice (Å)	Theoretical lattice (Å)	Expt. M_s at $T = 5\text{ K}$ ($\mu_B/f.u.$)	Theor. M_s ($\mu_B/f.u.$)	S-P M_s ($\mu_B/f.u.$)	T_c (K)
0	DO_{19}	$a = 5.1768(2)$ $c = 4.2246(3)$	$a = 5.134$ $c = 4.222$	6.55(9)	6.48	4.00	640
0	$L1_2^*$	$a = 3.6667(1)$	$a = 3.638$	6.55(9)	6.45	4.00	—
0.125	DO_{19}	$a = 5.1863(5)$ $c = 4.2298(5)$	$a = 5.146$ $c = 4.220$	5.88(2)	6.07	3.63	620(10)
0.125	$L2_1 + \text{DO}_{19}^*$	—	—	—	—	—	—
0.25	DO_{19}	$a = 5.1970(4)$ $c = 4.2395(3)$	$a = 5.159$ $c = 4.220$	5.33(3)	5.72	3.25	603(12)
0.25	$L2_1^\dagger$	$a = 5.7614(3)$	$a = 5.753$	3.91(3)	3.77	3.25	—
0.375	$L2_1^\dagger$	$a = 5.7623(3)$	$a = 5.767$	3.18(2)	—	2.88	590(9)
0.40	$L2_1^\dagger$	$a = 5.7626(1)$	—	3.09(3)	—	2.80	—
0.50	$L2_1^\dagger$	$a = 5.7632(3)$	$a = 5.788$	2.64(3)	2.47	2.50	509(8)
0.625	$L2_1^\dagger$	$a = 5.7640(4)$	$a = 5.802$	2.24(2)	—	2.13	450(5)
0.75	$L2_1^{*1}$	$a = 5.7653(6)$	$a = 5.806$	—	1.62	1.75	—

† annealed at 950°C for 7 days, ‡ annealed at 650°C for 25 days, * multi-phased samples.

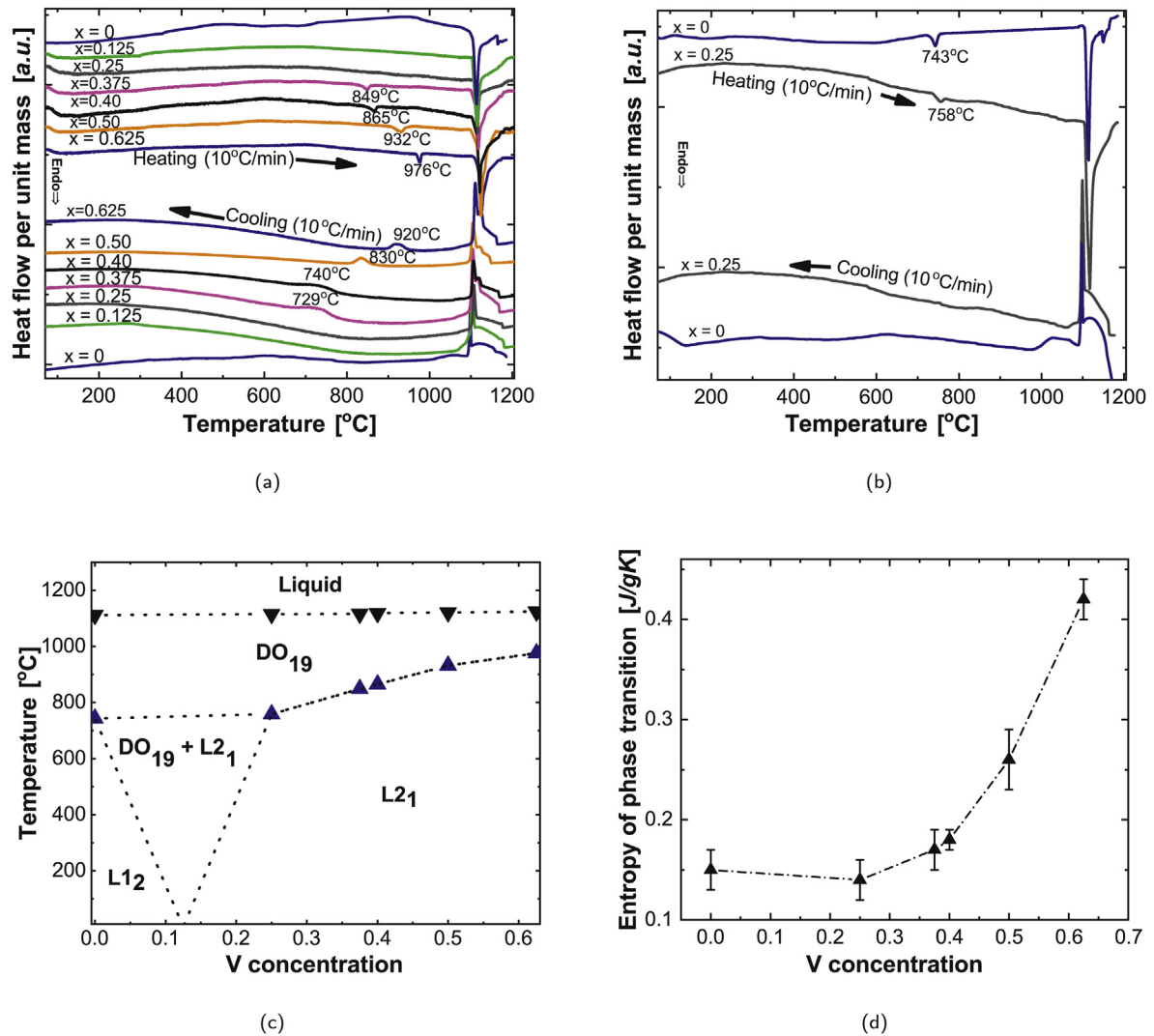


Fig. 7. (a) DSC scans of Fe_{3-x}V_xGe alloy series heat-treated at 950°C for 7 days measured at heating/cooling rate 10°C/min. (b) DSC scans for x = 0 and x = 0.25 heat-treated at 650°C for 25 days at heating/cooling rate 10°C/min. (c) Temperature versus V concentration phase diagram of Fe_{3-x}V_xGe alloy system. Martensitic phase transformation temperature: blue data pints, Melting point: red data points, and dashed lines: proposed phase boundaries. (d) The total entropy of phase transformation with V concentration.

annealed at 950°C for 7 days with different vanadium concentrations are presented in Table 4.

Thus, the L2₁ to DO₁₉ martensitic phase transformation is observed to depend on V concentration as well as annealing temperature conditions in off-stoichiometric Fe_{3-x}V_xGe intermetallic alloys, distinct from the temperature driven L1₂ to DO₁₉ transformation of the parent compound Fe₃Ge. After annealing at 950°C for 7 days, alloys for 0.375 ≤ x ≤ 0.75 are found to crystallize in the Heusler-like L2₁ structure, and alloys with 0 ≤ x ≤ 0.25, crystallize in the hexagonal DO₁₉ structure, which is the high temperature structure of the parent Fe₃Ge. On the other hand, alloys with 0.25 ≤ x ≤ 0.75 annealed at 650°C for 25 days are observed to crystallize in L2₁ structure. Clearly two distinct crystal structures are observed at room temperatures in x = 0.25; L2₁ for sample annealed at 650°C for 25 days and DO₁₉ for sample annealed at 950°C for 7 days, confirming the L2₁ to DO₁₉ *fcc* to *hcp* phase transformation, likely similar to those widely studied in cobalt and ferrous alloys [37,38]. According to the Shoji-Nishiyama mechanism, the atomic arrangements of the (111)_{fcc} plane and the (0001)_{hcp} planes are parallel [37]. Since, both *fcc* and *hcp* are close-packed structures, the only difference is in the stacking sequence of atoms normal to these

Table 4

The values T_1 , T_p , ΔS_p , and T_m of Fe_{3-x}V_xGe annealed at 950°C for 7 days measured in continuous heating at the rate 10°C/min. (The subscripts 1, p and m denote for onset, L2₁ to DO₁₉ transformation, and melting point, respectively.) The numbers in parentheses are the uncertainty in the last digit.

x	T_1 (°C)	T_p (°C)	ΔS_p (J/g·K)	T_m (°C)
0*	721	743	0.15(2)	1112
0.125	—	—	—	1115
0.25*	737	758	0.14(2)	1116
0.375	828	849	0.17(2)	1118
0.40	842	865	0.18(1)	1121
0.50	905	932	0.26(3)	1124
0.625	965	976	0.42(2)	1126

*Samples annealed at 650°C for 25 days.

planes. The transformation from *fcc* to *hcp* only requires the deformation of the atoms along the (111) plane to form a stacking sequence from *ABCABC* ... to *ABABAB* ... type [39].

3.4. Magnetic characterisation

The magnetic measurements for all single-phase samples were

done using the VSM module of a Quantum design PPMS Dynacool. Fig. 8(a) shows the field dependent magnetisation $M(H)$ curves of all stable samples in the $\text{Fe}_{3-x}\text{V}_x\text{Ge}$ series at 5 K. All the samples appeared to be ferromagnetic at 5 K. The saturation magnetising field is observed to decrease with increasing V content, though all samples are magnetically very soft. The saturation magnetic moments (M_s) were extracted from an Arrot plot [41], i.e., by extrapolating the linear part of M^2 versus to H/M to $H/M = 0$ (see inset to Fig. 8(a)). The extracted M_s at 5 K is observed to decrease linearly with increasing V content, however two different trendlines are observed (see Fig. 8(b)). This anomaly can be attributed due to different crystal structures (DO_{19} structure for low V content and L2_1 for high V content) consistent with our microstructural and XRD analysis. The extracted values of saturation magnetic moment (M_s) versus V concentration plot presented in Fig. 8(b) shows linear behaviour for all stable L2_1 phases, in good agreement with Slater-Pauling rule (shown in blue data points). The Slater-Pauling rule describes the dependence of the magnetic moment on the valence electron concentration (N_v) for ordered, half-metallic ferromagnetic Heusler compounds. This dependence is given by Ref. [4].

$$m = N_v - 24. \quad (1)$$

The slightly higher extracted saturation magnetic moments in the Fe rich members of L2_1 series are not unusual. Similar deviations from the theoretical values have been reported previously for Fe based Heusler compounds elsewhere [4,42]. The plot also shows linear behaviour for DO_{19} compositions, but the values are much higher than values from Slater-Pauling rule which simply indicates that the Slater-Pauling rule is not expected to hold for the hexagonal structure. Dramatic changes in magnetic moment are observed at $x = 0.25$ depending on the annealing condition, where we clearly observed two distinct pure crystal structures, DO_{19} for sample annealed at 950°C for 7 days and L2_1 for sample annealed at 650°C for 25 days. The red coloured solid square data point in Fig. 8(b) represents the magnetic moment for $x = 0.25$ (L2_1) annealed at 650°C for 25 days. All experimentally extracted saturation magnetic moments are in good agreement with those obtained from first-principle calculations (see Fig. 8(b)) (discussed in theory section below).

The high temperature magnetisation of a series of heat-treated

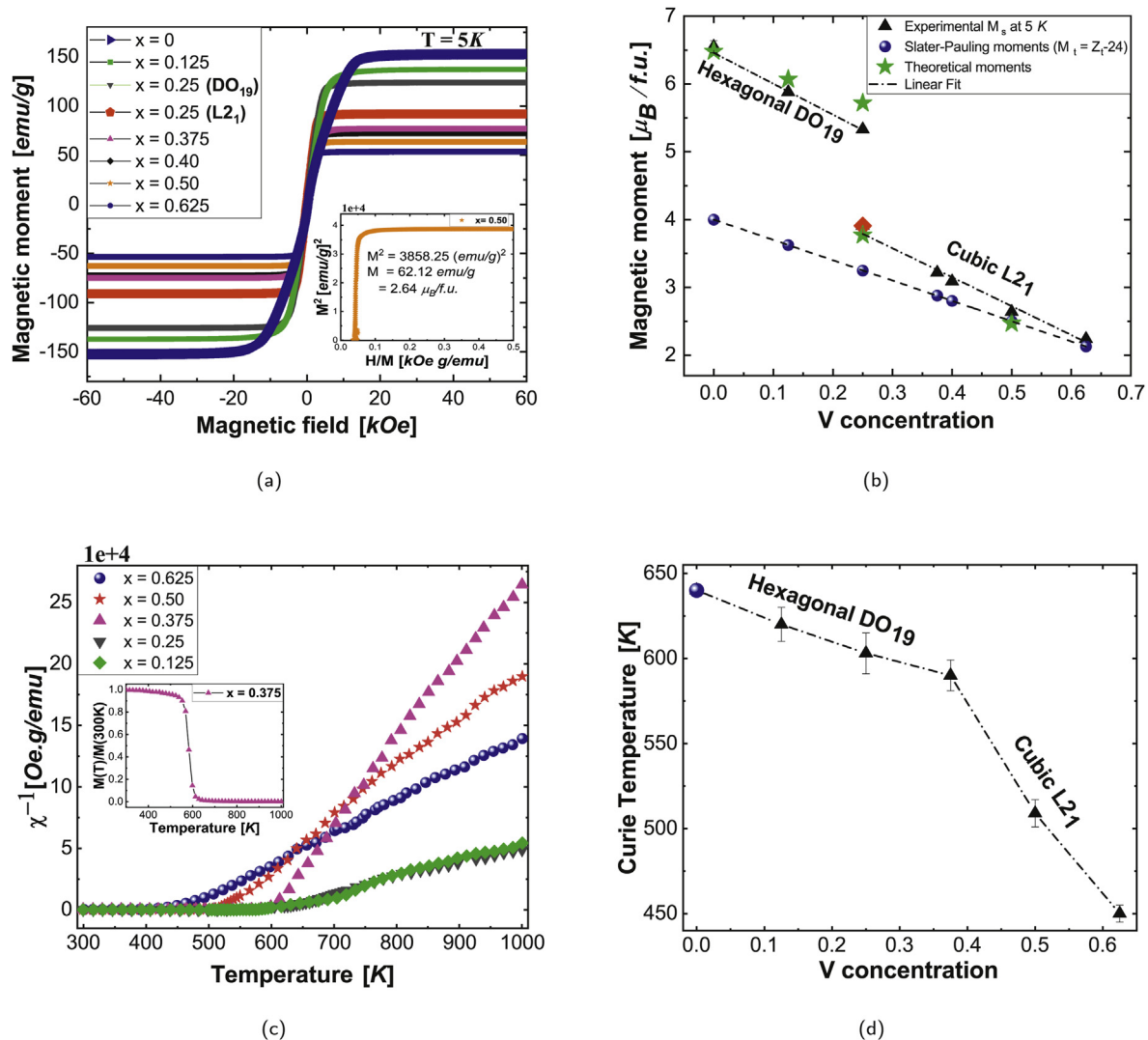


Fig. 8. (a) The field-dependent magnetisation at 5 K of $\text{Fe}_{3-x}\text{V}_x\text{Ge}$ alloy series annealed at 950°C for 7 days except the sample $x = 0.25$ (L2_1) which was annealed at 650°C for 25 days. The inset indicates the Arrot plot. (b) The magnetic moment versus V concentration both experimental and expected from Slater Pauling rule. (c) Inverse susceptibility as a function of temperature for the alloys ($0.125 \leq x \leq 0.625$) annealed at 950°C for 7 days. The inset is temperature dependent magnetisation for $x = 0.375$ with $H = 1000$ Oe. (d) The variation of T_c with V concentration (The blue data point is literature value of parent Fe_3Ge [21,40]).

$\text{Fe}_{3-x}\text{V}_x\text{Ge}$ alloy were measured by means of a vibrating sample magnetometer VSM equipped with a high temperature stage. The Curie temperatures of intermetallic alloy series were extracted taking the average of values obtained from linear fitting of the inverse susceptibility versus temperature graph as shown in Fig. 8(c) and the values obtained by plotting dM/dT as a function of temperature. The inset in Fig. 8(c) shows the specific magnetisation as a function of temperature for $x = 0.375$. The measurements were performed with a constant magnetic field of 1000 Oe in the temperature range of 300 K–1000 K. Even though the ferromagnetic Curie temperature T_c of these alloys are all observed to be above room temperature, and decrease with increasing x as shown in Fig. 8(d), the linear decrease of T_c of hexagonal samples $x = 0.125$ and $x = 0.25$ has different slope than that of cubic ones. The T_c values are well below the melting point and martensitic phase transition temperatures obtained by means of differential scanning calorimetry.

The saturation magnetic moments at 5 K and corresponding Curie temperature of all stable samples along with different annealing conditions for $\text{Fe}_{3-x}\text{V}_x\text{Ge}$ alloy series are presented in Table 3 above.

3.5. Electrical resistivity

The electrical resistivity data were collected using the van der Pauw method [43] in a PPMS Dynacool for samples with approximate dimensions $4 \times 4 \times 1.5 \text{ mm}^3$. Fig. 9 shows the temperature dependence of the electrical resistivity for $\text{Fe}_{3-x}\text{V}_x\text{Ge}$ measured during heating process in the temperature range from 5 K to 400 K. The electrical resistivity is observed to be sensitive to the composition change. An increase of V substitution for Fe is found to increase the residual resistivity that could be attributed due to atomic disorder arising from the substitution or sample quality. For $x = 0.25$ the variation of resistivity with temperature is purely metallic (see Fig. 9), but for higher V concentrations, a typical metallic behaviour is observed only for the low temperature range from 5 K up to 200 K. The resistivity is observed to saturate at higher temperatures for $x = 0.50$, suggesting a parallel contribution of the intrinsic resistivity and a weakly-varying shunting resistance, possibly due to grain boundaries [44,45]. The pseudo gap near Fermi level present in the minority spin channel of total density of state (see Fig. 13) for $x = 0.50$ might be responsible for this saturation effect. According to Allen and Chakraborty [45], the resistivity of a sub-band of electrons with an energy gap at the Fermi level is high and independent of temperature while the other sub-band has metallic character and resistivity increases with temperature and saturates at high temperature. The downturn in resistivity at higher temperature for $x = 0.625$ indicates the semiconducting nature of the material. This kind of anomalous behaviour of resistivity is quite similar to those observed in $\text{Fe}_{2-x}\text{V}_{1+x}\text{Al}$, $\text{Fe}_{2-x}\text{Ti}_{1+x}\text{Sn}$, $(\text{Fe}_{1-x}\text{V}_x)_3\text{Ga}$, and $(\text{Fe}_{1-x}\text{Ti}_x)_3\text{Ga}$ systems, where the tendency toward negative temperature dependence of electrical resistivity increases markedly with increasing x [46–49]. The anomaly that the resistivity reaches the maximum value quickly at $T \leq T_c$, decreases after that and reaches saturation at higher temperature is observed in many half-metallic Heusler alloys where the resistivity of one of the spin polarised sub-band with energy gap at Fermi level is expected to have a semiconductor character at high temperature [50–57]. The energy gap in down spin sub-band is observed to fall at Fermi level for $x = 0.75$ (see Fig. 13). The existence of a gap in one of the spin-polarised sub-band near Fermi level in total density of state for higher V concentration in $\text{Fe}_{3-x}\text{V}_x\text{Ge}$ can be considered as the anomalous decrease of resistivity with increasing temperature. Elucidating the true bulk transport properties unambiguously would ideally

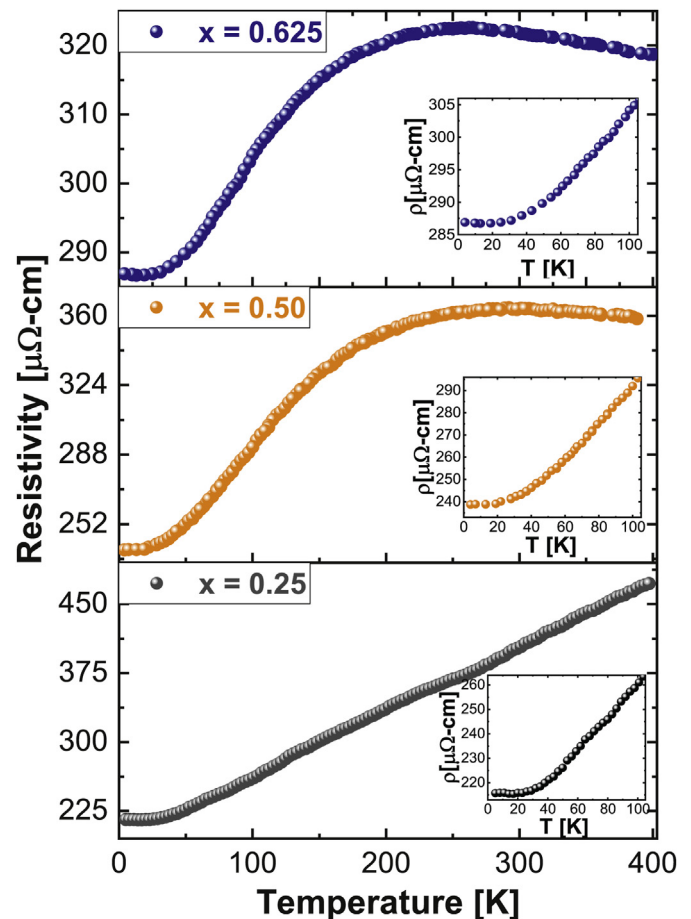


Fig. 9. Temperature dependence of electrical resistivity in $\text{Fe}_{3-x}\text{V}_x\text{Ge}$ ($x = 0.25, 0.50$, and 0.625 , all annealed at 950°C for 7 days respectively from bottom to top) in zero magnetic field.

require single crystal or highly ordered thin films.

3.6. Vickers micro hardness

During specimen preparation, we found the samples to be unusually hard, as evidenced by the polishing time required. For this reason, we decided to investigate the Vickers hardness of our alloy series, since most of the previous studies on mechanical properties are theoretical in nature [58–62] and only few are verified experimentally. The variation of Vickers micro hardness of our alloy series (all annealed at 950°C for 7 days) with V concentration is presented in Fig. 10 with corresponding values in Table 5. Hardness values reported are the averages of data taken from at least 12 different regions of each sample with 0.2 kg load and 10 s loading time. Relatively high hardness values are measured, approaching 10 GPa for $x = 1$, comparable with highest value 12 GPa reported for $\text{Co}_{2-x}\text{Ti}_x\text{FeGe}$ Heusler system [30] and higher than values reported for full Heuslers in the literature, e.g., $\sim 8.5 \text{ GPa}$ for powder Fe_2VAl [63], $\sim 8.5 \text{ GPa}$ for nanocrystalline Co_2FeAl [64], $\sim 7.3 \text{ GPa}$ and $\sim 7.9 \text{ GPa}$ for bulk polycrystalline Co_2MnGe and Co_2MnSi respectively [65]. The hardness is observed to increase almost linearly in going from hexagonal DO_{19} phases (with low V concentration) to L_{21} phases (with higher vanadium concentration) and depend on grains size and phases present as reported in the literature [66]. The grain size of the hexagonal phases at low V concentration are bigger than those of cubic phases at higher concentrations, and the cubic structure shows better toughness than the hexagonal structure,

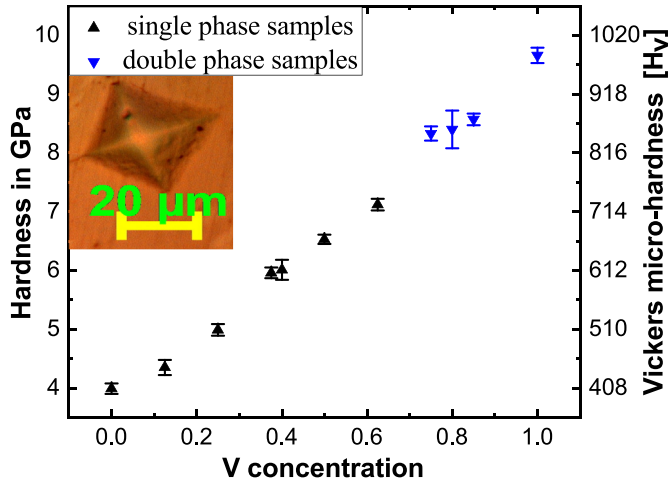


Fig. 10. Vickers hardness versus V concentration in $\text{Fe}_{3-x}\text{V}_x\text{Ge}$ with imprint of the indenter with radial cracks for $x = 0$ [top left]. The black data points represent the single phase compositions.

Table 5
Vicker's micro-hardness of the $\text{Fe}_{3-x}\text{V}_x\text{Ge}$ alloy series.

x	Vickers Hardness (GPa)
0	3.99 ± 0.09
0.125	4.35 ± 0.13
0.25	4.99 ± 0.10
0.3125	4.81 ± 0.37
0.375	5.96 ± 0.09
0.40	6.01 ± 0.17
0.50	6.53 ± 0.08
0.625	7.12 ± 0.10
0.75	8.33 ± 0.12
0.80	8.40 ± 0.32
0.85	8.57 ± 0.10
1	9.66 ± 0.13

presumably as the *fcc* structure has more slip planes in which the atoms are packed most closely relative to each other, and hence most tightly bonded to each other [67].

4. Theoretical calculations

4.1. Computational methodology

The Vienna Ab initio Simulation Package (VASP) was used for our density functional theory calculations (DFT) [68]. We used potentials from the projector augmented-wave (PAW) method and used the Perdew-Burke-Ernzerhof (PBE) functional [69–71]. The Monkhorst-Pack scheme was used to sample the Brillouin zone using a $9 \times 9 \times 9$ k-point grid for cubic structures and a $9 \times 9 \times 5$ grid for hexagonal structures in addition to a plane wave basis set with a cutoff energy of 400 eV [72]. Self-consistent field calculations of the total and projected electronic density of states were carried out with a Gaussian-type Fermi-level smearing width of 0.05 eV. To generate $\text{Fe}_{3-x}\text{V}_x\text{Ge}$ structures with varying V concentrations, we used the Special Quasi-random Structures (SQS) method implemented in the ATAT package [73,74]. The formation energy E_{form} (in eV/atom) of $\text{Fe}_{3-x}\text{V}_x\text{Ge}$ is defined as $E_{\text{form}} = (E_{\text{Fe}_{3-x}\text{V}_x\text{Ge}} - (1-x)E_{\text{Fe}_3\text{Ge}} - xE_{\text{V}_3\text{Ge}})$, where $E_{\text{Fe}_{3-x}\text{V}_x\text{Ge}}$ is the energy of a $\text{Fe}_{3-x}\text{V}_x\text{Ge}$ cell, $E_{\text{Fe}_3\text{Ge}}$ is the energy of a Fe_3Ge cell, and $E_{\text{V}_3\text{Ge}}$ is the energy of a V_3Ge cell, all per formula unit. We then normalised the x axis to start from $x = 0$ (Fe_3Ge) to $x = 1$ (Fe_2VGe). To obtain the charge distribution on the atoms in the simulation cells, we used

Bader charge analysis [75,76]. The VESTA program was used to visualise of atomic structures [77].

4.2. Theoretical results and discussion

Previously, first-principles DFT has been used to successfully calculate the electronic and magnetic properties of Heusler alloys [78–80]. In order to confirm experimental results and further investigate the electronic structure of this particular $\text{Fe}_{3-x}\text{V}_x\text{Ge}$ alloy system, we employed the Special Quasi-random Structures (SQS) method to generate structures between $x = 0$ and $x = 1$ for the L_{21} and DO_{19} phases. When comparing with experiment, we were able to generate structures with all of the same alloying ratios as Table 3 except $x = 0.40$ for the L_{21} phase. We note that for certain alloying ratios for the L_{21} phase such as $x = 0.375$, $x = 0.40$, and $x = 0.625$, the SQS method requires a larger supercell to preserve such concentrations. We propose that the SQS method being unable to create structures near $x = 0.40$ is due to the requirement of a significantly large supercell, beyond the capability of DFT. For $x = 0.375$ and $x = 0.625$, the quasi-random structures are forced to be confined to a rectangular supercell rather than a cubic supercell to preserve such alloying ratios without approaching the DFT limit (a much larger cubic supercell). However, from these rectangular structures, we are still able to obtain accurate lattice parameters to compare with experiment where only the long edges of the rectangular cell (*b*) are almost two times larger than the (*a*) lattice constant.

Fig. 11 shows the formation energy as a function of V concentration x of the L_{21} and DO_{19} phases respectively. The magnetic moment value is also depicted in the color axis of Fig. 11. We observe that at $x = 0.25$, the L_{21} phase is more energetically favourable than the DO_{19} phase. As expected for both phases, the increase of V concentration results in a decrease in magnetic moment with Fe_2VGe ($x = 1$) being the least magnetic alloying concentration. As can be seen in Table 3, calculated magnetic moments are in good agreement with the experimentally measured values. The calculated values of magnetic moment for $x = 0.375$ ($M_{S,\text{avg}} = 4.48 \mu_B$) and $x = 0.625$ ($M_{S,\text{avg}} = 3.61 \mu_B$) are almost $1 \mu_B$ bigger than the experimental results due to considered supercells being rectangular instead of cubic. For the lowest energy structure (most energetically favourable) at each experimentally observed alloying concentration, we calculated the electronic density of states (DOS). Fig. 13 depicts the atom projected DOS of the experimentally observed alloys for L_{21} ($x = 0.25$, $x = 0.375$, $x = 0.50$, $x = 0.625$, $x = 0.75$), DO_{19} ($x = 0$, $x = 0.125$, $x = 0.25$) and L_{12} ($x = 0$). The spin up and spin down contributions to the DOS are indicated by the black arrows. The insets of Fig. 13 also include the optimised geometry, the lattice constants and magnetic moment values (excluding M_S for $x = 0.375$ and $x = 0.625$) for the considered alloys. All the experimentally extracted lattice parameters are within $\sim 1\%$ of theoretical values (see Fig. 12). Because the experiments were done at a finite temperatures, this can cause the lattice parameters of the crystal structure to change from the 0 K structures due to the thermal expansion coefficient of the material and one might need longer annealing time yet to reach the true ground state. This also creates a margin of error such that all the structures generated with SQS lie in the range of thermal fluctuation at a given concentration. Due to this fact, we report an average value for lattice constant given at each concentration. In comparison to experiment, DFT calculations confirm that increasing V concentration increases the lattice constant on average (see Fig. 12). The metallic characteristics of the DO_{19} and L_{12} (for $x = 0$) Fe_3Ge structures arise from the orbital contribution of Fe atoms. Vanadium substitution can give different contributions to the density of states according to its position inside the material. For instance, if

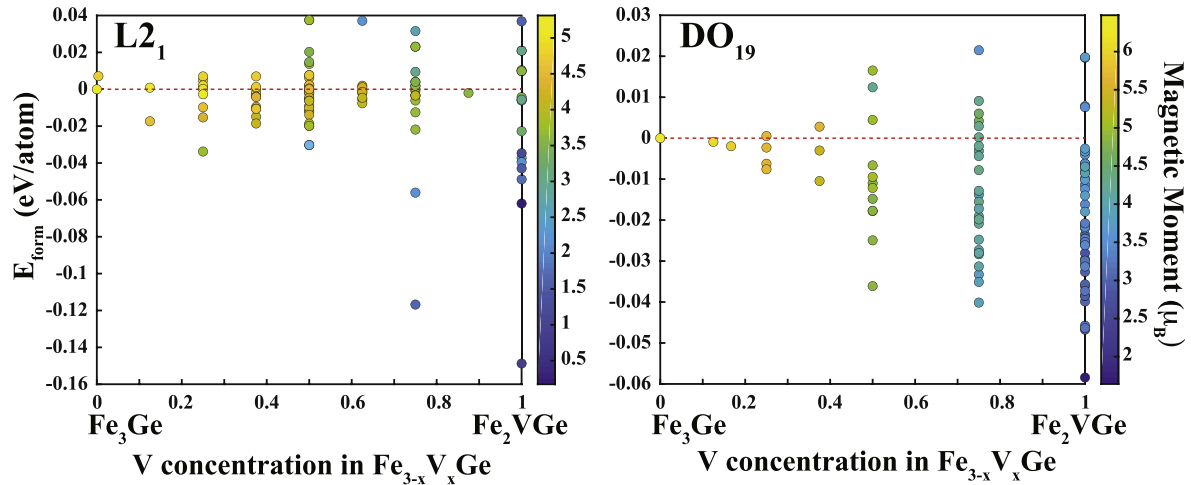


Fig. 11. The formation energy (in eV/atom) as a function of V concentration for the L2₁ and DO₁₉ alloys created with the SQS method. Each data point represents a different structure and the color axis indicates the magnetic moment value for each structure.

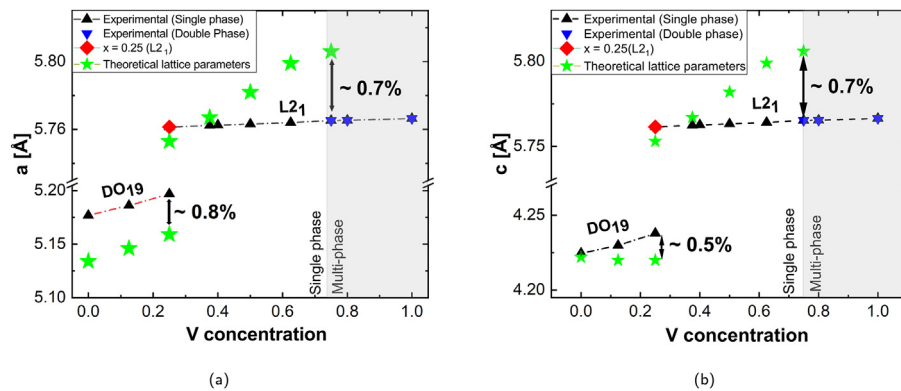


Fig. 12. Comparison plot between experimentally extracted lattice parameters and theoretical values from First-principles calculations of Fe_{3-x}V_xGe (a) *a* versus V concentration, and (b) *c* versus V concentration.

the V atom is positioned close to Ge atoms, it gives a contribution similar to the Ge contribution (see Fig. 13 L2₁ for $x = 0.50$, and $x = 0.75$). When V atoms are placed far from the Ge atoms, specifically if they are surrounded by Fe atoms, their DOS look similar to the DOS of Fe atoms (see Fig. 13 L2₁ for $x = 0.375$, $x = 0.50$, and $x = 0.625$). For the DO₁₉ structures, V atom substitution does not significantly effect the DOS of the bare Fe₃Ge structure due to low V concentration.

To understand the bonding type between the atoms and to gain insight on the electronic mechanism of these structures, we performed Bader charge transfer analysis of the Fe_{3-x}V_xGe alloys. Bader charge analysis indicates that while 0.10 electrons (e⁻) transfer to Ge from Fe atoms for L1₂, 0.30 e⁻ transfer for DO₁₉ at $x = 0$. This amount of electron transfer, in addition to the electronegativity difference between Fe and Ge atoms (0.18 according to the Pauling scale) indicate that there is non-polar covalent bonding between them. For DO₁₉ at $x = 0.125$ and $x = 0.25$, V (which has a lower electronegativity than Fe and Ge) loses 1.38 e⁻ and the three Ge atoms that are binding with this V atom gain 0.50 e⁻. Bader charge analysis for L2₁ at $x = 0$ indicates that charge transfer is different from DO₁₉ and L1₂ structures. Some Fe atoms which are binding with Ge donate 0.30 e⁻ and each Ge atoms take 0.13 e⁻ while some Fe atoms take 0.07 e⁻. With the substitution of V atoms instead of Fe atoms, polarisation increases between the Fe atoms. For $x = 0.50$, Fe atoms that are close to Ge atoms donate 0.35 e⁻

while the remaining Fe atoms gain 0.35 e⁻. The increasing of stability can be attributed to this increased polarisation.

5. Conclusion

In summary, an off-stoichiometric polycrystalline bulk Fe_{3-x}V_xGe intermetallic alloys series ($0 \leq x \leq 1$) was synthesised by arc-melting and the structural, magnetic, electrical transport and mechanical properties were investigated under different heat-treatment conditions. V substitution was observed to favour one of the Fe site in Fe₃Ge energetically to form L2₁ structure for higher V concentration and DO₁₉ structure for lower V concentrations, corroborated by first-principles calculations. The L2₁ to DO₁₉ martensitic phase transformation was observed to depend on V concentration as well as annealing conditions. DSC results also confirmed the diffusionless martensitic phase transformation in the alloy series. All the alloys in the series were found to be soft ferromagnets at 5 K with decreasing saturation magnetic moment with increasing V concentration. The sample with $x = 0.25$ crystallised in two different crystal structures L2₁ and DO₁₉ at two different annealing conditions, and they were found to exhibit two different saturation magnetisations at 5 K, with the magnetisation in the hexagonal phase being substantially larger. In contrast to DO₁₉ structures, the saturation magnetic moments of all L2₁ structures were observed to decrease linearly with V concentration

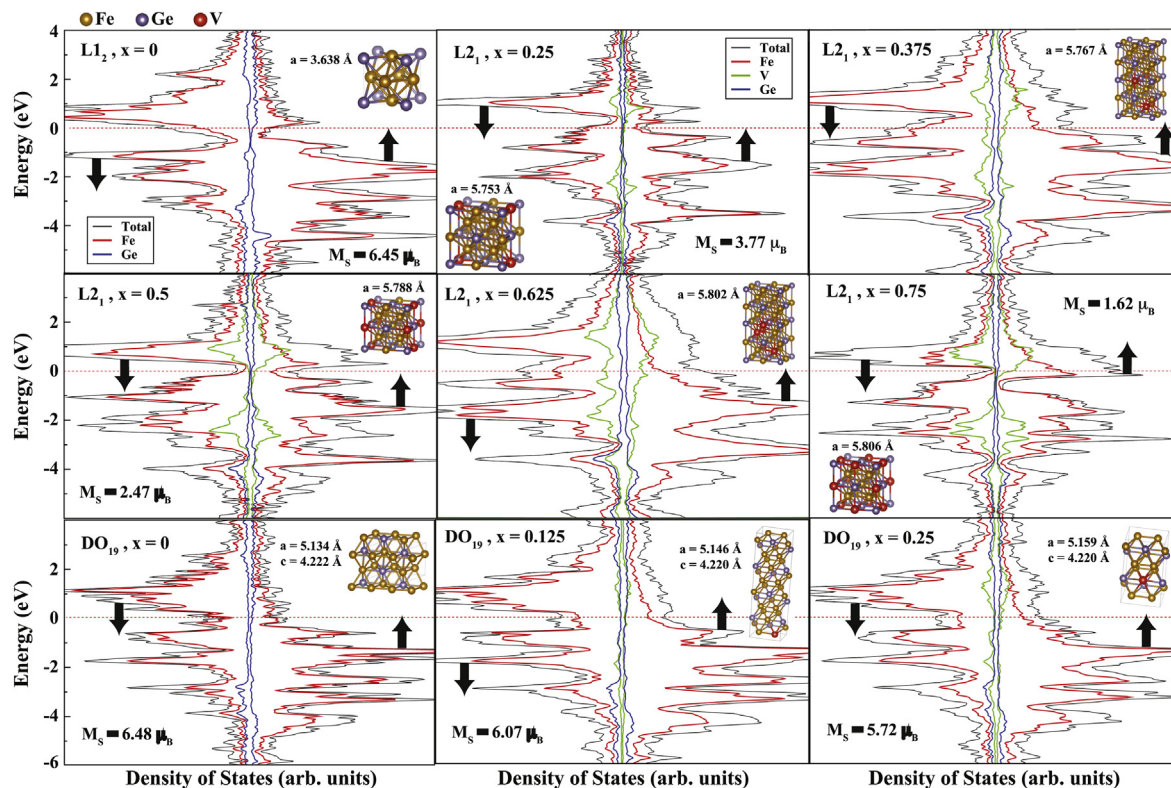


Fig. 13. The DOS and PDOS of the lowest energy structure at specific concentration ratios for L2₁, DO₁₉, and L1₂. The black arrows depict the spin up and spin down contributions and the red dotted line represents the Fermi level. The figure insets include the optimised structures, magnetic moment values and average lattice constants.

in close agreement with the expected Slater-Pauling values. The hexagonal samples were in all cases observed to have markedly higher values of saturation moments. The saturation magnetic moments extracted from experiment are found to be in good agreement with those obtained from first-principles calculations. The ferromagnetic Curie temperature T_c of these alloys were observed to decrease with increasing V concentration. The electrical resistivity measured over the temperature range from 5 K to 400 K showed a negative temperature coefficient of resistivity at high temperatures, more so with increasing the V concentration. The residual resistivity value is also found to increase with V substitution. Relatively high mechanical hardness values are also measured, increasing as V content increased. Vanadium is found to play a central role in tuning rich physical properties in $\text{Fe}_{3-x}\text{V}_x\text{Ge}$, changing the mechanical properties, stabilising the L2₁ structure not found in the parent Fe_3Ge compound, and shifting the martensitic transformation temperature to higher values compared to that of parent Fe_3Ge .

Declaration of competing interest

The authors declare that they have no known competing financial interests or personal relationships that could have appeared to influence the work reported in this paper.

CRediT authorship contribution statement

R. Mahat: Writing - original draft, Data curation, Formal analysis, Investigation. **Shambhu KC:** Writing - review & editing, Data curation, Formal analysis, Investigation. **D. Wines:** Writing - review & editing, Data curation, Formal analysis, Investigation. **F. Ersan:** Data curation, Formal analysis, Validation. **S. Regmi:** Data curation.

U. Karki: Data curation. **R. White:** Data curation, Formal analysis. **C. Ataca:** Funding acquisition, Project administration, Resources, Supervision, Validation. **P. Padhan:** Data curation. **A. Gupta:** Funding acquisition, Project administration, Resources, Supervision, Validation. **P. LeClair:** Conceptualization, Funding acquisition, Methodology, Project administration, Resources, Supervision, Validation, Writing - review & editing.

Acknowledgments

We would like to acknowledge Dr. Mark Weaver for helpful discussions on measurements of mechanical properties and for providing the instrument for hardness measurements. We would also like to acknowledge Mr. Bibekananda Das for helping us in carrying out high temperature magnetisation measurements. This work utilises the facilities offered by Central Analytical Facility (CAF) and MINT center of University of Alabama. We are thus grateful to the members of CAF and MINT center for helping us with measurements. The computational resources were provided by the UMBC High Performance Computing Facility (HPCF). The financial support to conduct this work was sourced from NSF DMREF Grant number 1235396, NSF DMR Grant number 1508680 and NSF DMR Grant number 1726213. The authors are thankful to NSF for providing the support to carry out this work.

Appendix A. Supplementary data

Supplementary data to this article can be found online at <https://doi.org/10.1016/j.jallcom.2020.154403>.

References

- [1] F. Heusler, Über magnetische manganlegierungen, *Verhandlungen Dtsch. Phys. Ges.* 5 (1903) 219.
- [2] C. Felser, G.H. Fecher, *Spintronics: from Materials to Devices*, Springer Science & Business Media, 2013.
- [3] F. Casper, C. Felser, R. Seshadri, C.P. Sebastian, R. Pöttgen, Searching for hexagonal analogues of the half-metallic half-Heusler XYZ compounds, *J. Phys. Appl. Phys.* 41 (3) (2008), 035002.
- [4] T. Graf, C. Felser, S.S. Parkin, Simple rules for the understanding of Heusler compounds, *Prog. Solid State Chem.* 39 (1) (2011) 1–50.
- [5] S.A. Khandy, D.C. Gupta, DFT investigations on mechanical stability, electronic structure and magnetism in Co_2TaZ ($Z = \text{Al, Ga, In}$) heusler alloys, *Semicond. Sci. Technol.* 32 (12) (2017) 125019.
- [6] L. Fan, F. Chen, C.-m. Li, X. Hou, X. Zhu, J.-l. Luo, Z.-Q. Chen, Promising spintronics: Mn-based Heusler alloys Mn_2Ga , Mn_2YGa ($Y = \text{V, Nb, Ta}$), ScMnVGa , *J. Magn. Magn. Mater.* 497 (2020) 166060.
- [7] Q. Zhang, H. Cui, C. Tian, H. Chen, J. Wang, H. Yuan, Thickness and composition dependencies of magnetization and perpendicular magnetic anisotropy of Heusler-like alloys based Mn_xGa — Co_2FeAl superlattices, *J. Alloys Compd.* 773 (2019) 327–337.
- [8] K.V. Shanavas, M.A. McGuire, D.S. Parker, Electronic and magnetic properties of Si substituted Fe_3Ge , *J. Appl. Phys.* 118 (12) (2015) 123902.
- [9] Y. Sakuraba, K. Izumi, T. Iwase, S. Bosu, K. Saito, K. Takanashi, Y. Miura, K. Futatsukawa, K. Abe, M. Shirai, Mechanism of large magnetoresistance in $\text{Co}_2\text{MnSi}/\text{Ag}/\text{Co}_2\text{MnSi}$ devices with current perpendicular to the plane, *Phys. Rev. B* 82 (2010), 094444.
- [10] T. Nakatani, N. Hase, H. Goripati, Y. Takahashi, T. Furubayashi, K. Hono, Co-based Heusler alloys for CPP-GMR spin-valves with large magnetoresistive outputs, *IEEE Trans. Magn.* 48 (5) (2012) 1751–1757.
- [11] K. Yakushiji, K. Saito, S. Mitani, K. Takanashi, Y. Takahashi, K. Hono, Current-perpendicular-to-plane magnetoresistance in epitaxial $\text{Co}_2\text{MnSi}/\text{Cr}/\text{Co}_2\text{MnSi}$ trilayers, *Appl. Phys. Lett.* 88 (22) (2006) 152204.
- [12] M. Kratochvílová, D. Král, M. Dušek, J. Valenta, R. Colman, O. Heczko, M. Veis, Fe_2MnSn -experimental quest for predicted heusler alloy, *J. Magn. Magn. Mater.* (2020) 166426.
- [13] F. Xin, C. You, H. Fu, L. Ma, Z. Cheng, N. Tian, Mechanically tuning magnetism and transport property in spin gapless semiconductor CoFeMnSi flexible thin film, *J. Alloys Compd.* 813 (2020) 152207.
- [14] T. Hahn, The 230 space groups, in: *International Tables for Crystallography Volume A: Space-Group Symmetry*, Springer, 2006, pp. 112–717.
- [15] M.J. Mehl, D. Hicks, C. Toher, O. Levy, R.M. Hanson, G. Hart, S. Curtarolo, The AFLOW library of crystallographic prototypes: part 1, *Comput. Mater. Sci.* 136 (2017) S1–S828.
- [16] X. Wang, Z. Cheng, Y. Jin, Y. Wu, X. Dai, G. Liu, Magneto-electronic properties and tetragonal deformation of rare-earth-element-based quaternary heusler half-metals: a first-principles prediction, *J. Alloys Compd.* 734 (2018) 329–341.
- [17] S. Keshavarz, N. Naghibolashrafi, M.E. Jamer, K. Vinson, D. Mazumdar, C.L. Dennis, W. Ratcliff II, J.A. Borchers, A. Gupta, P. LeClair, Fe_2MnGe : a hexagonal Heusler analogue, *J. Alloys Compd.* 771 (2019) 793–802.
- [18] A.F. Cabrera, F.H. Sánchez, Mössbauer study of ball-milled Fe-Ge alloys, *Phys. Rev. B* 65 (2002), 094202.
- [19] Q. Chen, A. Ngan, B. Duggan, An in-situ TEM study of the L_{12} to DO_{19} phase transformation in the intermetallic compound Fe_3Ge , *Intermetallics* 6 (2) (1998) 105–114.
- [20] Q. Chen, A. Ngan, B. Duggan, The $\text{L}_{12} \rightarrow \text{DO}_{19}$ transformation in the intermetallic compound Fe_3Ge , *J. Mater. Sci.* 33 (22) (1998) 5405–5414.
- [21] J. Drijver, S. Sinnema, F. Van der Woude, Magnetic properties of hexagonal and cubic Fe_3Ge , *J. Phys. F Met. Phys.* 6 (11) (1976) 2165.
- [22] H. Nakagawa, K. Kanematsu, Magnetic and X-Ray studies on $(\text{Fe}_{1-x}\text{V}_x)_3\text{Ge}$, *Japanese, J. Appl. Phys.* 18 (10) (1979) 1959.
- [23] A. Beitollahi, J. Booth, Structural and magnetic properties of $\text{Fe}_{3-x}\text{V}_x\text{Ge}$ alloys, *J. Phys. Condens. Matter* 2 (13) (1990) 2997.
- [24] K.v. Buschow, P. Van Engen, R. Jongebreur, Magneto-optical properties of metallic ferromagnetic materials, *J. Magn. Magn. Mater.* 38 (1) (1983) 1–22.
- [25] P. Walker, W.H. Tarn, *CRC Handbook of Metal Etchants*, CRC press, 1990.
- [26] C. Boudias, D. Monceau, *CaRIne Crystallography: the Crystallographic Software for Research and Teaching*, *CaRIne Crystallography*, 2006.
- [27] P. LeClair, X-ray Diffraction Calculation Software, 2018, <http://pleclair.ua.edu/XRD/>.
- [28] A. Putz, H. Brandenburg, Phase identification from power diffraction, *Crystal Impact Kreuzherrenstr.* 102, 53227 Bonn, Germany <https://www.crystalimpact.de/match>.
- [29] H.S. Nalwa, *Handbook of Nanostructured Materials and Nanotechnology*, Five-Volume Set, Academic Press, 1999.
- [30] S. KC, R. Mahat, S. Regmi, A. Mukherjee, P. Padhan, R. Datta, W.H. Butler, A. Gupta, P. LeClair, Tunable properties and potential half-metallicity in $(\text{Co}_2-x\text{Ti}_x)\text{FeGe}$ Heusler alloys: an experimental and theoretical investigation, *Phys. Rev. Mater.* 3 (2019) 114406.
- [31] M. Mohammadtaheri, A new metallographic technique for revealing grain boundaries in aluminum alloys, *Metallogr. Microstruct. Anal.* 1 (5) (2012) 224–226.
- [32] Y. El Hachi, B. Malard, S. Berveiller, J. Wright, Measurement of lattice rotations and internal stresses in over one hundred individual grains during a stress-induced martensitic transformation, in: *MATEC Web of Conferences* vol. 33, EDP Sciences, 2015, 02003.
- [33] H.P. Wijn, *Magnetic Properties of Metals: D-Elements, Alloys and Compounds*, Springer Science & Business Media, 2012.
- [34] B. Cullity, S. Stock, *Elements of X-Ray Diffraction*, 2014.
- [35] A.R. Denton, N.W. Ashcroft, Vegard's law, *Phys. Rev. A* 43 (1991) 3161–3164.
- [36] J.R. Rumble, *CRC Handbook of Chemistry and Physics*, 100th Edition, CRC Press, Internet Version 2019.
- [37] Z. Nishiyama, *Martensitic Transformation*, Elsevier, 2012.
- [38] R.M. Wentzcovitch, P.K. Lam, fcc-to-hcp transformation: a first-principles investigation, *Phys. Rev. B* 44 (1991) 9155–9158.
- [39] K. Manna, Y. Sun, L. Muechler, J. Kübler, C. Felser, Heusler, weyl and berry, *Nat. Rev. Mater.* 3 (8) (2018) 244.
- [40] T. Kaneko, T. Kanomata, Y. Kawazoe, Y. Uwatoko, *Magnetic Properties of D-Elements, Alloys and Compounds under Pressure*, Springer, 2014.
- [41] A. Arrott, Criterion for ferromagnetism from observations of magnetic isotherms, *Phys. Rev.* 108 (1957) 1394–1396.
- [42] S. Wurmel, G.H. Fecher, H.C. Kandpal, V. Ksenofontov, C. Felser, H.-J. Lin, Investigation of Co_2FeSi : the Heusler compound with highest Curie temperature and magnetic moment, *Appl. Phys. Lett.* 88 (3) (2006), 032503.
- [43] L.J. van der Pauw, A method of measuring specific resistivity and hall effect of discs of arbitrary shape, *Philips Res. Rep.* 13 (1) (1958) 1–9.
- [44] P.L. Rossiter, *The Electrical Resistivity of Metals and Alloys*, vol. 6, Cambridge University Press, 1991.
- [45] P. Allen, B. Chakraborty, Infrared and dc conductivity in metals with strong scattering: nonclassical behavior from a generalized Boltzmann equation containing band-mixing effects, *Phys. Rev. B* 23 (10) (1981) 4815.
- [46] Y. Nishino, M. Kato, S. Asano, K. Soda, M. Hayasaka, U. Mizutani, Semiconductorlike behavior of electrical resistivity in Heusler-type Fe_2VAl compound, *Phys. Rev. Lett.* 79 (1997) 1909–1912.
- [47] C.-S. Lue, Y.-K. Kuo, Thermal and transport properties of the Heusler-type compounds $\text{Fe}_{2-x}\text{Ti}_{1+x}\text{Sn}$, *J. Appl. Phys.* 96 (5) (2004) 2681–2683.
- [48] N. Kawamiya, Y. Nishino, M. Matsuo, S. Asano, Electrical-resistance maximum near the Curie point in $(\text{Fe}_{1-x}\text{V}_x)_3\text{Ga}$ and $(\text{Fe}_{1-x}\text{Ti}_x)_3\text{Ga}$, *Phys. Rev. B* 44 (1991) 12406–12412.
- [49] C.S. Lue, Y.-K. Kuo, Thermoelectric properties of the semimetallic Heusler compounds $\text{Fe}_{2-x}\text{V}_{1+x}\text{M}$ ($M = \text{Al, Ga}$), *Phys. Rev. B* 66 (2002), 085121.
- [50] N. Kourov, A. Korolev, V. Marchenkov, A. Lukoyanov, K. Belozeroval, Magnetic and electrical properties of the half-metallic ferromagnets Co_2CrAl , *Phys. Solid State* 55 (5) (2013) 977–985.
- [51] S. Majumdar, M. Chattopadhyay, V. Sharma, K. Sokhey, S. Roy, P. Chaddah, Transport properties of the ferromagnetic Heusler alloy Co_2TiSn , *Phys. Rev. B* 72 (1) (2005), 012417.
- [52] J. Barth, G.H. Fecher, B. Balke, S. Ouardi, T. Graf, C. Felser, A. Shkablo, A. Weidenkaff, P. Klaer, H.J. Elmers, et al., Itinerant half-metallic ferromagnets Co_2Ti ($Z = \text{Si, Ge, Sn}$): ab initio calculations and measurement of the electronic structure and transport properties, *Phys. Rev. B* 81 (6) (2010), 064404.
- [53] N. Kourov, V. Marchenkov, V. Pushin, K. Belozeroval, Electrical properties of ferromagnetic Ni_2MnGa and Co_2CrGa Heusler alloys, *J. Exp. Theor. Phys.* 117 (1) (2013) 121–125.
- [54] N. Kourov, A. Lukoyanov, V. Marchenkov, Specific features of the electrical resistance of half-metallic ferromagnetic alloys Co_2CrAl and Co_2CrGa , *Phys. Solid State* 55 (12) (2013) 2487–2490.
- [55] N. Kourov, V. Marchenkov, K. Belozeroval, H. Weber, Specific features of the electrical resistivity of half-metallic ferromagnets Fe_2MeAl ($\text{Me} = \text{Ti, V, Cr, Mn, Fe, Ni}$), *J. Exp. Theor. Phys.* 118 (3) (2014) 426–431.
- [56] H. Kurt, K. Rode, P. Stamenov, M. Venkatesan, Y.-C. Lau, E. Fonda, J. Coey, Cubic Mn_2Ga thin films: crossing the spin gap with ruthenium, *Phys. Rev. Lett.* 112 (2) (2014), 027201.
- [57] L. Jodin, J. Tobola, P. Pecheur, H. Scherrer, S. Kaprzyk, Effect of substitutions and defects in half-Heusler FeVsb studied by electron transport measurements and kkr-cpa electronic structure calculations, *Phys. Rev. B* 70 (2004) 184207.
- [58] M.I. Khan, H. Arshad, M. Rizwan, S. Gillani, M. Zafar, S. Ahmed, M. Shakil, Investigation of structural, electronic, magnetic and mechanical properties of a new series of equiatomic quaternary Heusler alloys CoYCrZ ($Z = \text{Si, Ge, Ga, Al}$): a DFT study, *J. Alloys Compd.* (2019) 152964.
- [59] S. Yousuf, D.C. Gupta, Insight into half-metallicity, spin-polarization and mechanical properties of L_{21} structured MnY_2Z ($Z = \text{Al, Si, Ga, Ge, Sn, Sb}$) Heusler alloys, *J. Alloys Compd.* 735 (2018) 1245–1252.
- [60] M. Elahmar, H. Rached, D. Rached, R. Khenata, G. Murtaza, S.B. Omran, W. Ahmed, Structural, mechanical, electronic and magnetic properties of a new series of quaternary Heusler alloys CoFeMnZ ($Z = \text{Si, As, Sb}$): a first-principle study, *J. Magn. Magn. Mater.* 393 (2015) 165–174.
- [61] K. Benkaddour, A. Chahed, A. Amar, H. Rozale, A. Lakdja, O. Benhelal, A. Sayede, First-principles study of structural, elastic, thermodynamic, electronic and magnetic properties for the quaternary Heusler alloys CoRuFeZ ($Z = \text{Si, Ge, Sn}$), *J. Alloys Compd.* 687 (2016) 211–220.
- [62] L. Zhang, X. Wang, Z. Cheng, Electronic, magnetic, mechanical, half-metallic and highly dispersive zero-gap half-metallic properties of rare-earth-element-based quaternary heusler compounds, *J. Alloys Compd.* 718 (2017) 63–74.
- [63] K.-D. Kim, C.-H. Lee, Fabrication and densification of Heusler Fe_2VAl alloy powders by mechanical alloying, *J. Korean Cryst. Growth Technol.* 23 (1) (2013) 51–57.

- [64] M. Hakimi, P. Kameli, H. Salamat, Y. Mazaheri, Evolution of microstructural and mechanical properties of nanocrystalline Co_2FeAl Heusler alloy prepared by mechanical alloying, *Powder Metall.* 56 (2) (2013) 111–116.
- [65] S. Ouardi, G.H. Fecher, B. Balke, A. Beleanu, X. Kozina, G. Stryganyuk, C. Felser, W. Klöß, H. Schrader, F. Bernardi, J. Morais, E. Ikenaga, Y. Yamashita, S. Ueda, K. Kobayashi, Electronic and crystallographic structure, hard x-ray photo-emission, and mechanical and transport properties of the half-metallic Heusler compound Co_2MnGe , *Phys. Rev. B* 84 (2011) 155122.
- [66] G. Rogl, A. Grytsiv, M. Gürth, A. Tavassoli, C. Ebner, A. Wünschek, S. Puchegger, V. Soprunyuk, W. Schranz, E. Bauer, et al., Mechanical properties of half-Heusler alloys, *Acta Mater.* 107 (2016) 178–195.
- [67] Z. Xie, S. Ni, M. Song, Effect of Y_2O_3 doping on FCC to HCP phase transformation in cobalt produced by ball milling and spark plasma sintering, *Powder Technol.* 324 (2018) 1–4.
- [68] G. Kresse, J. Furthmüller, Efficient iterative schemes for ab initio total-energy calculations using a plane-wave basis set, *Phys. Rev. B* 54 (1996) 11169–11186.
- [69] G. Kresse, D. Joubert, From ultrasoft pseudopotentials to the projector augmented-wave method, *Phys. Rev. B* 59 (1999) 1758–1775.
- [70] P.E. Blöchl, Projector augmented-wave method, *Phys. Rev. B* 50 (1994) 17953–17979.
- [71] J.P. Perdew, K. Burke, M. Ernzerhof, Generalized gradient approximation made simple, *Phys. Rev. Lett.* 77 (1996) 3865–3868.
- [72] H.J. Monkhorst, J.D. Pack, Special points for brillouin-zone integrations, *Phys. Rev. B* 13 (1976) 5188–5192.
- [73] A. Zunger, S.-H. Wei, L.G. Ferreira, J.E. Bernard, Special quasirandom structures, *Phys. Rev. Lett.* 65 (1990) 353–356.
- [74] A. van de Walle, Multicomponent multisublattice alloys, nonconfigurational entropy and other additions to the alloy theoretic automated toolkit, *Calphad* 33 (2) (2009) 266–278.
- [75] R.F.W. Bader, *Atoms in Molecules*, American Cancer Society, 2002.
- [76] G. Henkelman, A. Arnaldsson, H. Jónsson, A fast and robust algorithm for bader decomposition of charge density, *Comput. Mater. Sci.* 36 (3) (2006) 354–360.
- [77] K. Momma, F. Izumi, Vesta 3 for three-dimensional visualization of crystal volumetric and morphology data, *J. Appl. Crystallogr.* 44 (6) (2011) 1272–1276.
- [78] Y. Zhang, Z. Liu, Z. Wu, X. Ma, Prediction of fully compensated ferrimagnetic spin-gapless semiconducting FeMnGa/Al/In half Heusler alloys, *IUCr* 6 (4).
- [79] T. Samanta, S. Chaudhuri, S. Singh, V. Srihari, A. Nigam, P. Bhobe, Structural, electronic, magnetic, and transport properties of the equiatomic ni-based quaternary heusler alloys, *J. Alloys Compd.* (2019) 153029.
- [80] A. Candan, G. Ugur, Z. Charifi, H. Baaziz, M. Ellialtıoğlu, Electronic structure and vibrational properties in cobalt-based full-Heusler compounds: a first principle study of Co_2MnX ($\text{X} = \text{Si, Ge, Al, Ga}$), *J. Alloys Compd.* 560 (2013) 215–222.